Effects of nanofluid and radiative heat transfer on the double diffusive forced convection in microreactors

Lilian Govone [a], Mohsen Torabi [1,b], Linwei Wang [a], Nader Karimi [1,a,c]

[a] School of Engineering, University of Glasgow, Glasgow G12 8QQ, United Kingdom

[b] The George W. Woodruff School of Mechanical Engineering, Georgia Institute of Technology, Atlanta, GA 30332, USA

[c] Civil and Mechanical Engineering Department, University of Missouri-Kansas City, Kansas City, MO 64110, USA

Abstract

Understanding transport phenomena in microreactors remains challenging owing to the peculiar transfer features of microstructure devices and their interactions with chemistry. This paper, therefore, theoretically investigates heat and mass transfer in microreactors consisting of porous microchannels with thick walls, typical of real microreactors. To analyse the porous section of the microchannel the local thermal non-equilibrium model of thermal transport in porous media is employed. A first order, catalytic chemical reaction is implemented on the internal walls of the microchannel to establish the mass transfer boundary conditions. The effects of thermal radiation and nanofluid flow within the microreactor are then included within the governing equations. Further, the species concentration fields are coupled with that of the nanofluid temperature through considering the Soret effect. A semi-analytical methodology is used to tackle the resultant mathematical model with two different thermal boundary conditions. Temperature and species concentration fields as well as Nusselt number for the hot wall are reported versus various parameters such as porosity, radiation parameter and volumetric concentration of nanoparticles. The results show that radiative heat transfer imparts noticeable effects upon the temperature fields and consequently Nusselt number of the system. Importantly, it is observed that the radiation effects can lead to the development of a bifurcation in the nanofluid and porous solid phases and significantly influence the concentration field. This highlights the importance of including thermal radiation in thermo-chemical simulations of microreactors.

Keywords: Heat and mass transfer; Microreactor; Catalytic reaction; Soret number; Local thermal non-equilibrium; Nusselt number.

Nomenclature

a_{sf}	interfacial area per unit volume of porous media, m^{-1}	Sr	Soret Number
Bi	Biot number	T	Temperature, K
c	Concentration of the chemical products per unit volume, $\mathrm{mol. \, m}^{-3}$	T_1	Temperature of the lower solid material, K
$c_{p,nf}$	Specific heat of the fluid phase of the porous medium, $\mathrm{J. \, kg}^{-1}. \, \mathrm{K}^{-1}$	T_2	Temperature of the upper solid material, K
D	Diffusion coefficient , $\mathrm{m}^2. \, \mathrm{s}^{-1}$	T_c	Outer temperature of the upper solid material, K

---

[1] Corresponding authors.

E-mails: Mohsen.Torabi@my.cityu.edu.hk, Mohsen.Torabi@gatech.edu (M. Torabi), Nader.Karimi@glasgow.ac.uk (N.Karimi).

Da	Darcy number	T_H	Outer temperature of the lower solid material, K
D_T	Thermodiffusion coefficient ,$m^2.s^{-1}.K^{-1}$	T_{nf}	Temperature of the fluid phase of the porous medium, K
h_1	Height of the lower wall, m	T_s	Temperature of the solid phase of the porous medium, K
h_2	Height of the lower boundary of the upper wall, m	U_m	Average dimensionless velocity
h_3	Height of the upper boundary of the upper wall, m	u_p	Velocity of the fluid in porous medium, $m.s^{-1}$
h	External heat convection coefficient, $W.m^{-2}.K^{-1}$	U_p	Dimensionless velocity
h_{sf}	Internal heat convection coefficient, $W.m^{-2}.K^{-1}$	Y_1	Dimensionless height of the lower wall
k	Solid to fluid effective thermal conductivity ratio	Y_2	Dimensionless height of the upper wall lower boundary
k_1	Reference thermal conductivity for lower solid material, $W.m^{-1}.K^{-1}$	**Greek symbols**	
k_2	Reference thermal conductivity for upper solid material, $W.m^{-1}.K^{-1}$	γ	Damköhler number
k_{e1}	Ratio of the fluid to lower solid material thermal conductivities	ϵ	Porosity
k_{e2}	Ratio of the fluid to upper solid material thermal conductivities	θ	Dimensionless temperature
$k_{e,nf}$	Effective thermal conductivity of the nanofluid phase of the porous medium, $W.m^{-1}.K^{-1}$	θ_1	Dimensionless temperature of the lower solid material
k_{es}	Effective thermal conductivity of the solid phase of the porous medium, $W.m^{-1}.K^{-1}$	θ_2	Dimensionless temperature of the upper solid material
k_f	Thermal conductivity of the base fluid, $W.m^{-1}.K^{-1}$	θ_{nf}	Dimensionless temperature of the fluid phase of the porous medium
k_{nf}	Thermal conductivity of the nanofluid, $W.m^{-1}.K^{-1}$	$\theta_{nf,m}$	Dimensionless average temperature of the fluid phase of the porous medium
k_p	Thermal conductivity of the nanoparticles, $W.m^{-1}.K^{-1}$	θ_s	Dimensionless temperature of the solid phase of the porous medium
k_R	Kinetic constant, $m.s^{-1}$	θ_H	Dimensionless temperature at outer side of the lower wall
k_s	Thermal conductivity of the solid phase of the porous medium, $W.m^{-1}.K^{-1}$	κ	Permeability, m^2
N_c	dimensionless convection heat transfer (Case two)	κ^*	Rosseland mean absorption coefficient
Nu	Nusselt Number	μ_{eff}	Dynamic viscosity of porous medium, $Kg.s^{-1}.m^{-1}$
p	Pressure, Pa	μ_f	Dynamic viscosity of the base fluid, $Kg.s^{-1}.m^{-1}$
Q_1	Dimensionless volumetric internal heat generation rate for the lower solid material	μ_{nf}	Dynamic viscosity of the nanofluid, $Kg.s^{-1}.m^{-1}$
Q_2	Dimensionless volumetric internal heat generation rate for the upper solid material	ω_s	Dimensionless volumetric internal heat generation rate for the solid phase of the porous medium
Q_H	Dimensionless heat flux boundary condition (Case two)	ω_{nf}	Dimensionless volumetric internal heat generation rate for the fluid phase of the porous medium
$\dot{q}_1$	Volumetric internal heat generation rate for the lower solid material, $W.m^{-3}$	ρ	density of the fluid phase,$kg.m^{-3}$
$\dot{q}_2$	Volumetric internal heat generation rate for the upper solid material, $W.m^{-3}$	σ^*	Stefan-Boltzmann constant, $W.m^{-2}.K^{-4}$
q_H	Heat flux boundary condition (Case two), $W.m^{-2}$	ϕ	Dimensionless concentration
q_r	Radiation heat flux, $W.m^{-2}$		
Rd	Dimensionless radiation parameter		

1. Introduction

Recent advancements on the micro manufacturing techniques have resulted in miniaturised systems in different areas such as in heat transfer and chemical processes [1]. Although one of the main aims of using these techniques is to reduce the size of the system, micro thermal devices also provide higher surface to volume ratios, which lead to performance enhancements [1][2]. These advantages have promoted the development of microstructure chemical reactors [3][4]. Microreactors are used for process intensification and replacing batch reactors with continues processes in a variety of chemical industries including pharmaceutical and renewable energy industry [5][6].

In general, Microreactors can offer a superior control over the temperature compared to that of more conventional macro-reactors [3]. They normally consist of a bundle of micro porous channels, which allow more uniform temperature distribution within the system [7][8] and enable suppression of by-product formation [9]. Since microreactors offer massively increased surface to volume ratio and highly improved transport of heat and mass, they have been recognised as an attractive tool for processes with large heat of reactions [10]. This makes the radiation heat transfer an important mechanism of internal transport of energy within the system [11]. Further, microreactors often accommodate heterogeneous catalytic reactions [6]. Given the small size of these devices, an accurate prediction of the concentration field is of high significance in microreactor analysis [8]. This necessities consideration of the secondary modes of mass diffusion such as that caused by Soret effect, which in turn calls for an accurate thermal analyses. Nonetheless, the existing analyses of microreactors still largely ignore this potentially important part of the problem. This is especially true when the diffusion analysis is considered and the internal radiation heat transfer together with the thicknesses of the solid walls are incorporated into the simulations [12].

In microreactors the thickness of the solid walls can be comparable to the height of microchannels. The walls of microchannels have shown to have non-negligible impact on the thermal performances of the system [13][14]. Recently, a number of studies have examined the effects of walls on the thermal performance of chemically inert microchannels [15][16]. Extension of these to microreactors has been slow and only the most recent studies considered thick-wall microreactors [13][14]. Yet, addition of radiative effects to the conductive and convective modes of heat transfer in microreactors has remained as a totally unresolved issue.

In recent years, there have been a number of investigations on the thermal performances of porous microchannels. A pioneering investigation of the thermal behaviour of porous microchannels was performed by Torabi and Zhang [16]. In this study, heat transfer and entropy generation rate of magnetohydrodynamic forced convection in a porous channel with thick walls were reported. The local thermal equilibrium (LTE) model was used to analyse the porous section of the channel. Later, Elliott et al. [17][18] performed a similar task considering local thermal non-equilibrium (LTNE) approach for the thermal analysis of porous channels. These authors demonstrated that internal heat generations can result in major modifications of the temperature fields rendering deviation from local thermal equilibrium [17]. In a separate work, Elliott et al. [14] provided a comprehensive thermal and entropic analysis of porous microreactors in which solid walls were incorporated into the problem. Once again, LTNE model was used for the thermal analysis of the porous section of the reactor and internal heat generations were assumed within all parts of the system. It was shown that the impact of solid walls on the thermal performances of microchannels and microreactors can be significant [14][16]. It was therefore concluded that the usual practice of excluding solid walls from microreactor analysis is rather questionable. While fully porous-filled channels were considered in the initial analyses [14][16], Hunt et al. [13] opted in favour of partially-filled channels with thick walls. They also confirmed that the thickness of the walls had influential effects on the energetic and exergetic performances of microreactors.

Although not directly related to the present investigation, Torabi and co-workers [19][20] have examined the effects of solid sections of the system on the heat transfer and entropy generation analyses

of rotating solid cylindrical geometries. It was found that the radius of the cylinders, an indicator of the solid portion of the system, has a strong impact on the thermal behaviour of the system. Recently, there have been few numerical simulations of heat transfer and entropy generation within single phase flows in thick-wall microchannels [21][22]. These investigations [21][22] considered clear microchannels with various triangular cavities on the sidewalls. It was illustrated that by choosing the right value of Reynolds number in the microchannel, it is possible to achieve the minimum entropy generation rate [21]. Depending on the heat flux/temperature boundary conditions and internal heat generations, the radiation heat transfer can play a major role in heat transfer characterises of the system. Nevertheless, currently there is no study of the effects of this heat transfer mode upon the performance of microreactors [8][23].

All of the cited investigations only considered the transfer of heat and ignored the associated mass dispersion effects, which is clearly a shortcoming in transport analysis of microreactors. Generally, there exist various convection-diffusion investigations such as double diffusive convection phenomena in cavities with mass point sources [24] or double diffusive simulation of power-law fluids in porous cavities [25]. However, there are limited convection-diffusion investigations in connection to forced convection in microchannels. In a pertinent investigation, Sahu [26] investigated the double diffusive effects on the pressure-driven miscible flow in a channel. Sahu explored the effects of different viscosities for two different fluids on their stability mode and flow patterns resulting from the double diffusion phenomenon in the channel [26]. Later, the study of double diffusive convection in a planar channel [26] was extended to an axisymmetric pipe [27]. More recently, Torabi et al. [12] analysed forced convection-diffusion in porous microchannels by including Soret effects. Two types of channels, one with constant temperature boundary conditions and the other with heat flux and convection boundary conditions were examined. First order chemical reactions were assumed on the walls of the microchannel and LTE model was implemented in their work to analyse heat transfer within the porous section of the microchannel.

The present study is a comprehensive investigation of the effects of nanofluids and radiative heat transfer on the heat and mass transfer performance of a porous microreactor. This investigation extends the previous study of Torabi et al. [12] by employing the more accurate LTNE model in lieu of LTE approach and also considers a nanofluid flow in the porous section of the system. The rest of this paper is organised as follows. Section 2 has been divided into four subsections. Section 2.1 provides information about the geometry of the examined microreactors and the assumptions made throughout the analysis. Section 2.2 gives mathematical equations for the velocity, temperature and concentration fields. This subsection also provides the dimensionless parameters and governing equations. Section 2.3 deals with the solution of velocity, temperature and concentration fields and the validity of the solutions is discussed in section 2.4. A comprehensive discussion about the influences of various parameters on the temperature, concentration and Nusselt number of the system for both cases will be presented in section 3. Finally, section 4 concludes the outcomes of the paper.

2. Theoretical methods

2.1. Problem configuration and assumptions

Considering a microreactor which accommodates a heat generating/consuming fluid, such heat generation/consumption could be of physical or chemical nature [13][28]. The microreactor consists of a

bundle of microchannels fully filled by a porous medium and includes thick walls with constant, but distinctive, thermal conductivities, as shown in Fig. 1. The walls of the microchannel feature constant and uniform, but dissimilar internal heat generations. The internal heat generations within the solid walls could be, for instance, the result of absorption of microwave in the solid walls [29][30]. In the current analysis, it has been assumed that the fluid-solid interface boundary conditions inside the microchannel follow the continuum assumptions, which necessitate no velocity slip and no temperature jump [13]. Two types of outer boundary conditions are considered for the microchannel. Case one (Fig. 1a), assumes that the upper and lower surfaces are subject to constant but different temperatures. Case two (Fig. 1b) includes a constant heat flux on the lower wall and a convective boundary condition on the upper wall.

In the current work, the classical macroscopic theory of transport in porous media [31] is employed and therefore pore scale phenomena [32][33] are not investigated. The following assumptions are made throughout the proceeding analyses.

- The porous medium is assumed to be homogenous and isotropic, fluid saturated and includes uniform and steady internal heat generation representing the absorption of electromagnetic waves.
- The fluid flow is laminar, steady and incompressible, with uniform heat generation/consumption.
- The porous system is under local thermal non-equilibrium condition.
- Fully developed conditions are assumed throughout the microreactor.
- Due to the sub-millimetre transversal dimension of the microchannel the Rayleigh number is small and thus free convection is ignored [34][8].
- Physical properties such as porosity, specific heat, density and thermal conductivity are constant.
- A single step, first order, catalytic reaction occurs on the internal walls of the microchannel and the resultant species diffuse into the nanofluid through Fickian and Soret mechanisms [35].
- Sharp reaction zones are excluded and hence axial conduction of heat can be neglected in the current study [36].
- It is assumed that the temperature of the solid phase of the porous medium is high enough to include the effect of radiation on the temperature distribution [37].

2.2. Governing equations

The transport of momentum in the microchannel is modelled by Darcy-Brinkman equation. This reads

$$-\frac{\partial p}{\partial x} + \mu_{eff}\frac{d^2 u_p}{dy^2} + \frac{\mu_{nf}}{\kappa}u_p = 0 \quad h_1 \leq y \leq h_2 \tag{1}$$

in which $\mu_{eff} = \frac{\mu_{nf}}{\epsilon}$ is the effective viscosity of the nanofluid. The transport of thermal energy in different components of the microreactor is given by the following set of equations.

$$k_1\frac{\partial}{\partial y}\left(\frac{\partial T_1}{\partial y}\right) + \dot{q}_1 = 0 \quad 0 \leq y \leq h_1 \tag{2a}$$

$$k_{e,nf}\frac{\partial^2 T_{nf}}{\partial y^2} + h_{sf}a_{sf}(T_s - T_{nf}) + s_{nf} = \rho c_p u_p\frac{\partial T_{nf}}{\partial x} \quad h_1 \leq y < h_2 \tag{2b}$$

$$k_{es}\frac{\partial^2 T_s}{\partial y^2} + h_{sf}a_{sf}(T_s - T_{nf}) + s_s - \frac{\partial q_r}{\partial y} = 0 \quad h_1 < y \leq h_2 \tag{2c}$$

$$k_2\frac{\partial}{\partial y}\left(\frac{\partial T_2}{\partial y}\right) + \dot{q}_2 = 0 \quad h_2 \leq y \leq h_3 \tag{2d}$$

5

These, respectively, correspond to the bottom wall, the nanofluid and solid phases within the porous region and the top wall. The mass dispersion equation, coupled with the temperature of the nanofluid through Soret effect, can be written as follows

$$D \frac{\partial^2 c}{\partial y^2} + D_T \frac{\partial^2 T_{nf}}{\partial y^2} = 0 \quad h_1 \leq y < h_2 \tag{3}$$

The radiation parameter takes the form of [38]

$$q_r = \frac{-4 \sigma^*}{3 \kappa^*} \frac{\partial T_s^4}{\partial y}, \tag{4}$$

and using Rosseland approximation [38] the last term on the left hand side of the energy transport for nanofluid, Eq. (2b), reduces to

$$\frac{\partial q_r}{\partial y} = -\frac{16\sigma^* T_0^3}{3 \kappa^*} \frac{\partial^2 T_s}{\partial y^2} \tag{5}$$

The two sets of thermal boundary conditions are implemented. These include,

Case one:

$$y = 0 \quad T_1 = T_H \tag{6a}$$

$$y = h_3 \quad T_2 = T_c \tag{6b}$$

Case two:

$$y = 0 \quad -k_1 \frac{dT_1}{dy} = q_H \tag{7a}$$

$$y = h_3 \quad -k_2 \frac{dT_2}{dy} = h(T_2 - T_c) \tag{7b}$$

It is important to recall that advection in the axial direction can be neglected in this analysis. This is due to the implementation of the outer thermal boundary conditions, which highly strengthens the transversal transport and hence renders the axial transport relatively insignificant [39]. The validity of this argument has been demonstrated in a large number of recent investigations, see for example [17][40][41][42][43][16]. In particular, this assumption is very realisable in the limit of low Peclet number, which is frequently encountered in microreactors [3]. Hence, the provided system of energy Eq. (2) is transformed to the following set of equations:

$$k_1 \frac{\partial}{\partial y}\left(\frac{\partial T_1}{\partial y}\right) + \dot{q}_1 = 0 \quad 0 \leq y \leq h_1 \tag{8a}$$

$$k_{e,nf} \frac{\partial^2 T_{nf}}{\partial y^2} + h_{sf} a_{sf}(T_s - T_{nf}) + s_{nf} = 0 \quad h_1 \leq y < h_2 \tag{8b}$$

$$k_{es} \frac{\partial^2 T_s}{\partial y^2} + h_{sf} a_{sf}(T_s - T_{nf}) + s_s - \frac{\partial q_r}{\partial y} = 0 \quad h_1 < y \leq h_2 \tag{8c}$$

$$k_2 \frac{\partial}{\partial y}\left(\frac{\partial T_2}{\partial y}\right) + \dot{q}_2 = 0 \quad h_2 \leq y \leq h_3 \tag{8d}$$

In both cases, the following interface conditions are implemented for the closure of the system [44][45]

$$y = h_1 \quad u_p = 0 \quad T_1 = T_s = T_{nf}$$

$$k_1 \frac{dT_1}{dy}\bigg|_{y=h_1} = k_{e,nf} \frac{dT_{nf}}{dy}\bigg|_{y=h_1} + k_{es} \frac{dT_s}{dy}\bigg|_{y=h1} + \frac{16\sigma^* T_0^3}{\kappa^*} \frac{dT_s}{dy}\bigg|_{y=h1}, \quad D \frac{dc}{dy}\bigg|_{y=h_1} = -k_R c. \tag{9a}$$

$$y = h_2 \quad u_p = 0 \quad T_2 = T_s = T_{nf}$$

$$k_2 \frac{dT_2}{dy}\bigg|_{y=h_2} = k_{e,nf} \frac{dT_{nf}}{dy}\bigg|_{y=h_2} + k_{es} \frac{dT_s}{dy}\bigg|_{y=h2} + \frac{16\sigma^* T_0^3}{\kappa^*} \frac{dT_s}{dy}\bigg|_{y=h2}, \quad D \frac{dc}{dy}\bigg|_{y=h_2} = k_R c. \tag{9b}$$

The following dimensionless parameters are next introduced.

$$\theta_1 = \frac{T_1}{T_C} \quad \theta_s = \frac{T_s}{T_C} \quad \theta_f = \frac{T_{nf}}{T_C} \quad \theta_2 = \frac{T_2}{T_C} \quad Y = \frac{y}{h_3} \quad Y_1 = \frac{h_1}{h_3}$$

$$Y_2 = \frac{h_2}{h_3} \quad Q_1 = \frac{\dot{q}_1 h_3{}^2}{k_1 T_C} \quad Q_2 = \frac{\dot{q}_2 h_3{}^2}{k_2 T_C} \quad Q_H = \frac{q_H h_3}{k_1 T_C} \quad w_f = \frac{s_f h_3{}^2}{k_{es} T_C}$$

$$w_s = \frac{s_s h_3{}^2}{k_{es} T_C} \quad U_p = \frac{u_p}{u_r} \quad Da = \frac{\kappa}{h_3{}^2} \quad k = \frac{k_{es}}{k_{enf}} = \frac{(1-\varepsilon)k_s}{\varepsilon k_f} \tag{10}$$

$$Bi = \frac{h_{sf} a_{sf} h_3{}^2}{k_{es}} \quad Br = \frac{\mu_f u_r{}^2}{T_C k_{es}} \quad k_{e1} = \frac{k_{ef}}{k_1} \quad k_{e2} = \frac{k_{ef}}{k_2} \quad Nc = \frac{hh_3}{k_2}$$

$$\phi = \frac{c}{c_0} \quad Sr = \frac{D_T T_C}{D c_0} \quad \gamma = \frac{k_R h_3}{D} \quad Rd = \frac{16\sigma^* T_0^3}{3\kappa^* k_{es}}$$

where $u_r = -\frac{h_3^2}{\mu_f}\frac{\partial p}{\partial x}$.

Substituting from Eq. (10) into the momentum equations leads to the following dimensionless equation for the transport of momentum.

$$1 + \frac{C_\mu}{\epsilon}\frac{d^2 U_p}{dY^2} - \frac{C_\mu}{Da}U_p = 0 \quad Y_1 < Y \le Y_2 \tag{11}$$

Repeating the same algebraic process for the energy Eqs. (8a-d) results in the following dimensionless equations.

$$\frac{d^2\theta_1}{dY^2} + Q_1 = 0 \quad 0 \le Y \le Y_1 \tag{12a}$$

$$\left(\frac{C_k}{k}\right)\frac{d^2\theta_{nf}}{dY^2} + Bi(\theta_s - \theta_{nf}) + w_{nf} = 0 \quad Y_1 < Y \le Y_2 \tag{12b}$$

$$(1 + Rd)\frac{d^2\theta_s}{dY^2} - Bi(\theta_s - \theta_{nf}) + w_s = 0 \quad Y_1 \le Y < Y_2 \tag{12c}$$

$$\frac{d\theta_2}{dY^2} + Q_2 = 0 \quad 0 \le Y \le Y_2 \tag{12d}$$

where $\frac{k_{nf}}{k_f} = C_k$ and $\frac{\mu_{nf}}{\mu_f} = C_\mu$.

In the present investigation C_μ and C_k can be any temperature-independent models for the ratios of viscosity and thermal conductivity of nanofluid to those of the base fluid, respectively. Two commonly used empirical models are chosen here [46][47][15]:

$$C_k = 1 + \frac{3\left(\frac{k_p}{k_f}-1\right)\varphi}{\left(\frac{k_p}{k_f}+2\right)-\left(\frac{k_p}{k_f}-1\right)\varphi}, \tag{13a}$$

and

$$C_\mu = \frac{1}{(1-\varphi)^{2.5}}. \tag{13b}$$

The nanofluid is assumed to be water-copper or any other nanofluid that can be described with the model that is used in this investigation. The dimensionless dispersion equation can be written as:

$$\frac{d^2\phi}{dY^2} + Sr\frac{d^2\theta_{nf}}{dY^2} = 0 \; ; Y_1 \le Y < Y_2 \tag{14}$$

Further, the thermal boundary conditions (6) and (7) are converted to the following relations.

Case one:

$$Y = 0 \quad \theta_1 = \theta_H \tag{15a}$$

$$Y = 1 \quad \theta_2 = 1 \tag{15b}$$

Case two:

$$Y = 0 \quad -\frac{d\theta_1}{dY} = Q_H \tag{16a}$$

$$Y = 1 \quad -\frac{d\theta_2}{dY} = Nc(\theta_2 - 1) \tag{16b}$$

The non-dimensional thermal and hydrodynamic interface conditions for the two cases are given by [24, 25, 30]

$$Y = Y_1 \quad U_p = 0 \quad \theta_1 = \theta_s = \theta_{nf}$$

$$\left.\frac{d\theta_1}{dY}\right|_{Y=Y_1} = C_k k_{e1} \left.\frac{d\theta_{nf}}{dY}\right|_{Y=Y_1} + k(1 + Rd)k_{e1} \left.\frac{d\theta_s}{dY}\right|_{Y=Y_1} \quad \left.\frac{d\phi}{dY}\right|_{Y=Y_1} = -\gamma\phi, \tag{17a}$$

$$Y = Y_2 \quad U_p = 0 \quad \theta_2 = \theta_s = \theta_{nf}$$

$$\left.\frac{d\theta_2}{dY}\right|_{Y=Y_2} = C_k k_{e2} \left.\frac{d\theta_{nf}}{dY}\right|_{Y=Y_2} + k(1 + Rd)k_{e2} \left.\frac{d\theta_s}{dY}\right|_{Y=Y_2} \quad \left.\frac{d\phi}{dY}\right|_{Y=Y_2} = \gamma\phi. \tag{17b}$$

Algebraic manipulation of these equations and boundary conditions renders a set of fourth-order differential equations for the solid and nanofluid phases inside the porous region. These are given by

$$C_k(1 + Rd)\theta_s''''(Y) - \text{Bi}(C_k + k(1 + Rd))\theta_s''(Y) - \text{Bi}k\left(w_f + w_s\right) = 0, \tag{18}$$

$$C_k(1 + Rd)\theta_{nf}''''(Y) - \text{Bi}(C_k + k(1 + Rd))\theta_{nf}''(Y) - \text{Bi}k\left(w_f + w_s\right) = 0. \tag{19}$$

Using the dimensionless parameters defined by the Eq. (10), the dimensionless Nusselt number is written as

$$Nu = \frac{2\epsilon(Y_2 - Y_1)\left.\frac{\partial\theta}{\partial Y}\right|_{Y=Y_1}}{k_{e1}(\theta_f(Y1) - \theta_{nfm})}, \tag{20}$$

where,

$$\theta_{nfm} = \frac{1}{(Y_2 - Y_1)U_m} \int_{Y_1}^{Y_2} U_p \theta_f \, dY, \tag{21}$$

and,

$$U_m = \frac{1}{(Y_2 - Y_1)} \int_{Y_1}^{Y_2} U_p \, dY. \tag{22}$$

2.3. Velocity, temperature and concentration profiles

Analytical solution of the dimensionless momentum Eq. (11) results in the following velocity profile for the fluid velocity within the porous region.

$$U_p(Y)$$

$$= \frac{Da\left(\cosh(-Y_1 Z) - \cosh\left(Z(Y - (Y_1 + Y_2))\right) + \cosh(Y_2 Z) - \cosh(ZY)\right)}{C_\mu\left(\sinh(ZY_1) + \cosh(ZY_1) + \sinh(ZY_2) + \cosh(ZY_2)\right)}$$

$$+ \frac{Da\left(-\sinh(-Y_1 Z) + \sinh\left(Z(Y - (Y_1 + Y_2))\right) + \sinh(Y_2 Z) - \sinh(ZY)\right)}{C_\mu\left(\sinh(ZY_1) + \cosh(ZY_1) + \sinh(ZY_2) + \cosh(ZY_2)\right)}, \tag{23}$$

where $Z = \frac{\sqrt{\epsilon}}{\sqrt{Da}}$.

The equations governing the transport of thermal energy in the system (Eqs. (12a) and (12d), and Eqs. (18) and (19)) are then solved analytically. These give the following general solutions for the temperature fields in the solid walls of the microreactor as well as those of the solid and nanofluid phases within the porous medium.

$$\theta_1(Y) = -\frac{Q_1}{2}Y^2 + B_1 Y + C_1, \tag{23a}$$

$$\theta_s(Y) = -\frac{k(\omega_s + \omega_{nf})}{2(C_k + k(1 + Rd))}Y^2 + F_s \cosh(Y\Gamma) + G_s\sinh(Y\Gamma) + K_{1s}Y + K_{2s,} \tag{24b}$$

$$\theta_{nf}(Y) = -\frac{k(\omega_s + \omega_{nf})}{2(C_k + k(1 + Rd))}Y^2 + F_f \cosh(Y\Gamma) + G_f\sinh(Y\Gamma) + K_{1f}Y + K_{2f,} \tag{24c}$$

$$\theta_2(Y) = -\frac{Q_2}{2}Y^2 + B_2Y + C_2, \tag{24d}$$

where $\Gamma = \sqrt{\frac{Bi(C_k + k(1 + Rd))}{C_k(1 + Rd)}}$.

Solution of the normalised dispersion equation Eq. (14) yields the following concentration profile of the chemical species in the conduit:

$$\phi(Y) = -\frac{k(\omega_s + \omega_{nf})}{2(C_k + k(1 + Rd))}Y^2 + F_f \cosh(Y\Gamma) + G_f \sinh(Y\Gamma) + BY + A. \tag{25}$$

Finding the particular solution requires incorporation of the boundary and interface conditions Eqs. (15)-(17). The algebraic manipulations for deriving the constant parameters in Eqs. (24a-d) and (25) are cumbersome and lengthy and hence for conciseness reasons they are not shown in here.

2.4. Validation

To ensure the validity of the mathematical model developed in this section, the predicted temperature fields and Nusselt numbers for $R_d = 0$ and an ordinary fluid were compared to those reported by Elliott et al. [17]. This resulted in identical graphs and therefore demonstrated the correctness of the current model.

3. Results and discussion

This section is divided into three parts. The first one is a discussion about the temperature profiles of the system under investigation. The second part puts forward a discussion about the Nusselt number and the third subsection focuses on the concentration profiles. As the hydrodynamics of porous channels are well studied in the literature [14][13], velocity distributions have not been illustrated for the sake of brevity. Further, this work concerns with the effects of internal thermal radiation and nanofluid on the performance of the microreactors. Thus, the temperature and concentration fields and also Nusselt number are primarily analysed against variations in the thermal radiation and concentration of nanoparticles. It is worth noting that within the rest of this paper parts a and b of each figure correspond, respectively, to Case 1 and 2 shown in Figs. 1a and 1b. It should be also recalled that in temperature illustrations, the solid and dashed lines represent the temperature of the solid and fluid components of the porous section, respectively. In this section the parametric values listed in Table 1 are used, unless otherwise stated.

Table 1: Default values of the configurational and thermophysical parameters.

$\epsilon = 0.9$	$Da = 0.0001$	$Q_1 = 1$	$\varphi = 0.04$
$Bi = 0.5$	$\theta_h = 2$	$Q_2 = 1$	$\gamma = 0.1$
$Y_1 = 0.2$	$\omega_s = 2$	$k_{e1} = 0.5$	$N_C = 1$
$Y_2 = 0.8$	$\omega_{nf} = 2$	$k_{e2} = 0.5$	$Q_h = 1$
$Rd = 2$	$k = 0.5$	$Sr = 0.5$	

3.1. Temperature fields

Figure 2 depicts the temperature fields for both cases with different values of radiation parameters. A comparison between the two parts of this figure reveals that the temperature fields are more sensitive to the radiation parameter in the second case. This is because of the fact that in the second case the boundary conditions do not impose a specific temperature on the outer walls, and hence provide more flexibility for the temperature distribution. Fig. 2b shows that increasing the radiation parameter decreases the temperature of the system. Such behaviour is in good agreement with those reported in the previous investigations [12]. However, Fig. 2a shows that increasing the radiation parameter decreases the temperature within the lower part and increases the temperature within the upper part of the system. It is also observed that the radiation effect tends to initially reduce the temperature difference between the nanofluid and porous solid phase. Further increase in the radiation parameter eliminates the local temperature difference and eventually renders a bifurcation in which the nanofluid becomes locally cooler than the porous solid. This is a new finding and has not been previously reported in the open literature. A physical explanation can be provided for this behaviour. As shown in Eq. (12b), inclusion of Rosseland approximation converts thermal radiation into an added conductivity of the solid phase of the porous medium. Thus, by increasing the radiation parameter the solid phase becomes more capable of losing heat. Yet, the capacity of exchanging thermal energy with the nanofluid is dominated with the interphase Biot number [44][47], which has remained unchanged in the current formulation. Thus, most of the extra heat loss from the solid phase is not received by the nanofluid of the system. It is emphasised that this conclusion is valid within the limit of the assumptions made in the current investigation. Further details of radiation should be included before a general quantitative statement can be made about the radiative effects upon the thermal characteristics of microreactors. Nonetheless, the present analysis clearly reflects the significance of thermal radiation in the prediction of temperature fields in microreactors.

Figure 3 shows the effects of volumetric concentration of the nanoparticles on the temperature fields of the two investigated cases. Figure 3a. indicates that since the upper and lower bounds of the microreactor have been fixed with constant temperatures, the nanoparticles volume concentration does not have an influential impact on the temperature distribution. However, increasing the nanoparticles volume fraction on the nanofluid phase decreases the temperature of the system components in Case 2. As it has been shown in Fig. 3b, increasing the volume concentration may marginally increase the temperature of the upper wall of the system. This is due to the fact that more heat is crossing through this wall and is transfer by convection to the upper environment. Figure 4 represents the temperature distributions for both cases with different internal heat generation rates. It is seen that increasing the magnitude of the internal heat generation results in augmenting the temperature difference between the fluid and solid phases of the porous section. This is somehow similar to the findings of the previous works [14][28]. Nevertheless, due to the inclusion of radiation effect in the current work the deviation from LTE in heat generating cases is less pronounced.

3.2. Nusselt number

Figure 5 illustrates the variation of Nusselt number versus radiation parameter for different values of porosity for two investigated cases. This figure shows that increasing either of porosity or radiation parameter of the system, increases the Nusselt number on the lower wall of the microchannel. This is to be expected, as increasing the porosity or radiation parameter intensifies the heat flux on the lower wall. As observed in the previous subsection, this tends to decrease the temperature of the system. The trend of the Nusselt number versus radiation is almost linear for both cases, which is clearly seen in Fig. 5. Figure 6 is a companion to Fig. 5, which illustrates the variation of Nusselt number versus nanoparticles volumetric concentration for different values of porosity of the porous medium. Similar to the Fig. 5, Fig. 6 show that increasing the volumetric concentration of nanoparticles increases the Nusselt number on the lower wall of the channel. The growth in Nusselt number is due to a general decrease of temperature within the system, which increases the capacity of heat convection. This finding is also in keeping with those reported in the recent studies of forced convection of nanofluids in porous media [47][15].

3.3 Concentration fields

Figures 7-9 illustrate the effects of mass transfer parameters including Soret and Damköhler numbers and also the radiation parameter upon the concentration of the species within the system. Figure 7 depicts the profiles of concentration across the microchannel for different values of Soret number. The general form of these profiles clearly indicates the diffusion of species from the catalytic surfaces located on the internal walls of the microchannel. In Fig. 7 Soret number has been varied in a relatively small range. Yet, this figure clearly shows that the concentration field responds strongly to these small changes in Soret number. Mathematically, increasing the value of Soret number increases the effects of the second derivative of the nanofluid temperature within the concentration field on the basis of Eq. (14) and consequently increases the concentration of chemical species. Since the radiation parameter tends to decrease the temperature of the system, increasing the radiation parameter leads to reducing the concentration of species for both cases. This is well illustrated in Fig. 8. As shown in Fig. 2, increasing the radiation parameter from four to eight has less impact on the temperature field compared with the corresponding effect when the radiation parameter increases from zero to four. Consequently, increasing the radiation parameter from four to eight in Fig. 8 results in much less effect upon the concentration field in comparison with when the radiation parameter grows from zero to four. This strong non-uniformity in the temperature and concentration responses to the radiative characteristics of the system is of practical importance. In a microreactor, the chemical processes can be temperature dependent through the temperature dependency of the chemical kinetics. Further, the production rate is strongly dependent upon the concentration field. The current results show that both of these fields are strongly affected by the thermal radiation in a non-uniform way. Hence, inclusion of a representative radiation model in the simulations of microreactors is an important necessity. Figure 9 shows the effect of Damköhler number on the concentration field for Cases 1 and 2. Increasing the Damköhler parameter may be interpreted as decreasing the diffusive power of the system, and hence decreases the concentration field within the channel. It should be clarified that the concentration field is coupled with the second derivative of the nanofluid temperature based on Eq. (14). The value of this derivation on the lower wall for different cases

is only slightly different. Therefore the reported concentration fields in Figs. 7-9 are largely similar for the two investigated cases.

4. Conclusions

This investigation considered double diffusive forced convection in a porous microreactor when the solid walls' thicknesses are included within the system. The LTNE model of thermal transport was applied on the porous section of the system and a first order, catalytic chemical reaction was implemented as the concentration boundary conditions. The governing equations were solved using a combined analytical-numerical solution technique. A comprehensive analysis of temperature, Nusselt number and concentration profiles were then provided. It was found that the radiation parameter decreases the temperature of the system, and consequently increases the Nusselt number on the hot wall. As the temperature profile of Case 2 has more room to vary compared with Case 1, the effects of radiation parameter and the volumetric concentration of nanoparticles were more influential on the transport characteristics of Case 2. Importantly, for the first time, it was shown that increasing the radiation parameter of the porous solid phase can result in a bifurcation in the temperature fields of the system. It was also shown that due to the effect of the second derivative of the nanofluid temperature, the concentration field for both cases are very similar. The consequences of these on the modelling of practical microreactors were subsequently discussed.

Acknowledgment

References

[1]   Walther DC, Ahn J. Advances and challenges in the development of power-generation systems at small scales. Prog Energy Combust Sci 2011;37:583–610. doi:10.1016/j.pecs.2010.12.002.

[2]   Dincer I, Rosen MA. Thermal Energy Storage, Systems and Applications. 2nd ed. Wiley; 2011.

[3]   Roberge DM, Ducry L, Bieler N, Cretton P, Zimmermann B. Microreactor technology: A revolution for the fine chemical and pharmaceutical industries? Chem Eng Technol 2005;28:318–23. doi:10.1002/ceat.200407128.

[4]   Haber J, Kashid MN, Borhani N, Thome J, Krtschil U, Renken A, et al. Infrared imaging of temperature profiles in microreactors for fast and exothermic reactions. Chem Eng J 2013;214:97–105. doi:10.1016/j.cej.2012.10.021.

[5]   Yao X, Zhang Y, Du L, Liu J, Yao J. Review of the applications of microreactors. Renew Sustain Energy Rev 2015;47:519–39. doi:10.1016/j.rser.2015.03.078.

[6]   Kolb G. Review: Microstructured reactors for distributed and renewable production of fuels and electrical energy. Chem Eng Process Process Intensif 2013;65:1–44. doi:10.1016/j.cep.2012.10.015.

[7]   Chou SK, Yang WM, Li J, Li ZW. Porous media combustion for micro thermophotovoltaic system applications. Appl Energy 2010;87:2862–7. doi:10.1016/j.apenergy.2009.06.039.

[8]   Torabi M, Karimi N, Peterson GP, Yee S. Challenges and progress on the modeling of entropy generation in porous media: A review. Int J Heat Mass Transf 2017;114:31–46. doi:http://dx.doi.org/10.1016.

[9] Tanimu A, Jaenicke S, Alhooshani K. Heterogeneous catalysis in continuous flow microreactors: A review of methods and applications. Chem Eng J 2017;327:792–821. doi:10.1016/j.cej.2017.06.161.

[10] Guettel R, Turek T. Assessment of micro-structured fixed-bed reactors for highly exothermic gas-phase reactions. Chem Eng Sci 2010;65:1644–54. doi:10.1016/j.ces.2009.11.002.

[11] Ju Y, Maruta K. Microscale combustion: Technology development and fundamental research. Prog Energy Combust Sci 2011;37:669–715. doi:10.1016/j.pecs.2011.03.001.

[12] Torabi M, Torabi M, Peterson GP. Entropy generation of double diffusive forced convection in porous channels with thick walls and Soret effect. Entropy 2017;19:171. doi:10.3390/e19040171.

[13] Hunt G, Karimi N, Torabi M. Analytical investigation of heat transfer and classical entropy generation in microreactors - The influences of exothermicity and asymmetry. Appl Therm Eng 2017;119:403–24. doi:10.1016/j.applthermaleng.2017.03.057.

[14] Elliott A, Torabi M, Karimi N. Thermodynamics analyses of porous microchannels with asymmetric thick walls and exothermicity: An entropic model of microreactors. J Therm Sci Eng Appl 2017;9:41013. doi:10.1115/1.4036802.

[15] Dickson C, Torabi M, Karimi N. First and second law analyses of nanofluid forced convection in a partially-filled porous channel – The effects of local thermal non-equilibrium and internal heat sources. Appl Therm Eng 2016;103:459–80. doi:10.1016/j.applthermaleng.2016.04.095.

[16] Torabi M, Zhang K. Temperature distribution, local and total entropy generation analyses in MHD porous channels with thick walls. Energy 2015;87:540–54. doi:10.1016/j.energy.2015.05.009.

[17] Elliott A, Torabi M, Karimi N, Cunningham S. On the effects of internal heat sources upon forced convection in porous channels with asymmetric thick walls. Int Commun Heat Mass Transf 2016;73:100–10. doi:10.1016/j.icheatmasstransfer.2016.02.016.

[18] Elliott A, Torabi M, Hunt G, Karimi N. Erratum to "On the effects of internal heat sources upon forced convection in porous channels with asymmetric thick walls" [Int. Comm. Heat Mass Trans. 73 (2016) 100–110]. Int Commun Heat Mass Transf 2017;85:76–80. doi:10.1016/j.icheatmasstransfer.2017.05.002.

[19] Torabi M, Zhang K. First and second thermodynamic laws analyses between and inside two rotating solid cylindrical geometries with magnetohydrodynamic flow. Int J Heat Mass Transf 2015;89:760–9. doi:10.1016/j.ijheatmasstransfer.2015.05.101.

[20] Torabi M, Zhang K, Shohel M. Temperature and entropy generation analyses between and inside two rotating solid cylindrical geometries using copper-water nanofluid. J Heat Transfer 2015;137:51701. doi:10.1115/1.4029596.

[21] Li YF, Xia GD, Ma DD, Jia YT, Wang J. Characteristics of laminar flow and heat transfer in microchannel heat sink with triangular cavities and rectangular ribs. Int J Heat Mass Transf 2016;98:17–28. doi:10.1016/j.ijheatmasstransfer.2016.03.022.

[22] Zhai YL, Xia GD, Liu XF, Li YF. Exergy analysis and performance evaluation of flow and heat transfer in different micro heat sinks with complex structure. Int J Heat Mass Transf 2015;84:293–303. doi:10.1016/j.ijheatmasstransfer.2015.01.039.

[23] Torabi M, Zhang K, Karimi N, Peterson GP. Entropy generation in thermal systems with solid

structures – A concise review. Int J Heat Mass Transf 2016;97:917–31. doi:10.1016/j.ijheatmasstransfer.2016.03.007.

[24]   Serrano-Arellano J, Gijón-Rivera M, Riesco-Ávila JM, Elizalde-Blancas F. Numerical study of the double diffusive convection phenomena in a closed cavity with internal CO2 point sources. Int J Heat Mass Transf 2014;71:664–74. doi:10.1016/j.ijheatmasstransfer.2013.12.078.

[25]   Kefayati GR. Simulation of double diffusive natural convection and entropy generation of power-law fluids in an inclined porous cavity with Soret and Dufour effects (Part I: Study of fluid flow, heat and mass transfer). Int J Heat Mass Transf 2016;94:539–81. doi:10.1016/j.ijheatmasstransfer.2015.05.058.

[26]   Sahu KC. Double diffusive effects on pressure-driven miscible channel flow: Influence of variable diffusivity. Int J Multiph Flow 2013;55:24–31. doi:10.1016/j.ijmultiphaseflow.2013.03.005.

[27]   Bhagat KD, Tripathi MK, Sahu KC. Instability due to double-diffusive phenomenon in pressure-driven displacement flow of one fluid by another in an axisymmetric pipe. Eur J Mech B/Fluids 2016;55:63–70. doi:10.1016/j.euromechflu.2015.08.006.

[28]   Torabi M, Karimi N, Zhang K. Heat transfer and second law analyses of forced convection in a channel partially filled by porous media and featuring internal heat sources. Energy 2015;93:106–27. doi:10.1016/j.energy.2015.09.010.

[29]   Chen WH, Cheng TC, Hung CI. Modeling and simulation of microwave double absorption on methanol steam reforming for hydrogen production. Int J Hydrogen Energy 2011;36:333–44. doi:10.1016/j.ijhydene.2010.09.009.

[30]   Chen WH, Cheng TC, Hung CI. Numerical predictions on thermal characteristic and performance of methanol steam reforming with microwave-assisted heating. Int J Hydrogen Energy 2011;36:8279–91. doi:10.1016/j.ijhydene.2011.04.145.

[31]   Civan F. Porous Media Transport Phenomena. John Wiley & Sons; 2011.

[32]   Torabi M, Peterson GP, Torabi M, Karimi N. A thermodynamic analysis of forced convection through porous media using pore scale modeling. Int J Heat Mass Transf 2016;99:303–16. doi:10.1016/j.ijheatmasstransfer.2016.03.127.

[33]   Torabi M, Torabi M, Peterson GP. Heat transfer and entropy generation analyses of forced convection through porous media using pore scale modeling. J Heat Transfer 2017;139:12601. doi:10.1115/1.4034181.

[34]   Nield DA, Bejan A. Convection in Porous Media. 4th editon. New York: Speringer; 2013.

[35]   Matin MH, Pop I. Forced convection heat and mass transfer flow of a nanofluid through a porous channel with a first order chemical reaction on the wall. Int Commun Heat Mass Transf 2013;46:134–41. doi:10.1016/j.icheatmasstransfer.2013.05.001.

[36]   Chen J, Song W, Gao X, Xu D. Hetero-/homogeneous combustion and flame stability of fuel-lean propane–air mixtures over platinum in catalytic micro-combustors. Appl Therm Eng 2016;100:932–43. doi:http://dx.doi.org/10.1016/j.applthermaleng.2016.02.122.

[37]   Wang P, Vafai K, Liu DY. Analysis of radiative effect under local thermal non-equilibrium conditions in porous media-application to a solar air receiver. Numer Heat Transf Part A Appl 2014;65:931–48. doi:10.1080/10407782.2013.850917.

[38] Modest MF. Radiative Heat Transfer. Elsevier; 2013. doi:10.1016/B978-0-12-386944-9.50022-4.

[39] Kaisare NS, Vlachos DG. A review on microcombustion: Fundamentals, devices and applications. Prog Energy Combust Sci 2012;38:321–59. doi:10.1016/j.pecs.2012.01.001.

[40] Torabi M, Peterson GP. Effects of velocity slip and temperature jump on the heat transfer and entropy generation in micro porous channels under magnetic field. Int J Heat Mass Transf 2016;102:585–95. doi:10.1016/j.ijheatmasstransfer.2016.06.080.

[41] Ibáñez G, López A, Pantoja J, Moreira J. Combined effects of uniform heat flux boundary conditions and hydrodynamic slip on entropy generation in a microchannel. Int J Heat Mass Transf 2014;73:201–6. doi:10.1016/j.ijheatmasstransfer.2014.02.007.

[42] Ibáñez G. Entropy generation in MHD porous channel with hydrodynamic slip and convective boundary conditions. Int J Heat Mass Transf 2015;80:274–80. doi:10.1016/j.ijheatmasstransfer.2014.09.025.

[43] Ibáñez G, López A, Pantoja J, Moreira J. Entropy generation analysis of a nanofluid flow in MHD porous microchannel with hydrodynamic slip and thermal radiation. Int J Heat Mass Transf 2016;100:89–97. doi:http://dx.doi.org/10.1016/j.ijheatmasstransfer.2016.04.089.

[44] Karimi N, Agbo D, Talat Khan A, Younger PL. On the effects of exothermicity and endothermicity upon the temperature fields in a partially-filled porous channel. Int J Therm Sci 2015;96:128–48. doi:10.1016/j.ijthermalsci.2015.05.002.

[45] Yang K, Vafai K. Analysis of temperature gradient bifurcation in porous media – An exact solution. Int J Heat Mass Transf 2010;53:4316–25. doi:10.1016/j.ijheatmasstransfer.2010.05.060.

[46] Mashaei PR, Shahryari M, Madani S. Numerical hydrothermal analysis of water-Al2O3 nanofluid forced convection in a narrow annulus filled by porous medium considering variable properties: Application to cylindrical heat pipes. J Therm Anal Calorim 2016;126:891–904. doi:10.1007/s10973-016-5550-3.

[47] Torabi M, Dickson C, Karimi N. Theoretical investigation of entropy generation and heat transfer by forced convection of copper–water nanofluid in a porous channel — Local thermal non-equilibrium and partial filling effects. Powder Technol 2016;301:234–54. doi:10.1016/j.powtec.2016.06.017.
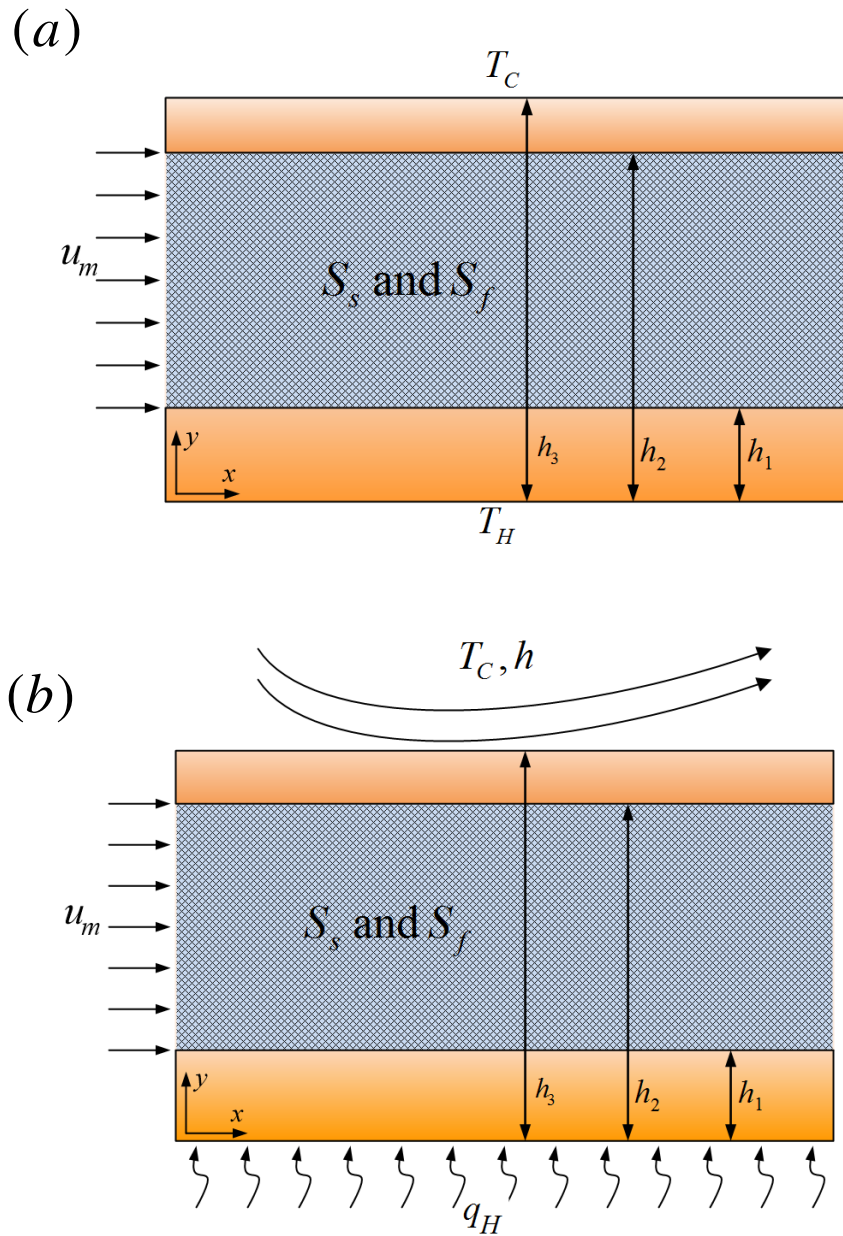
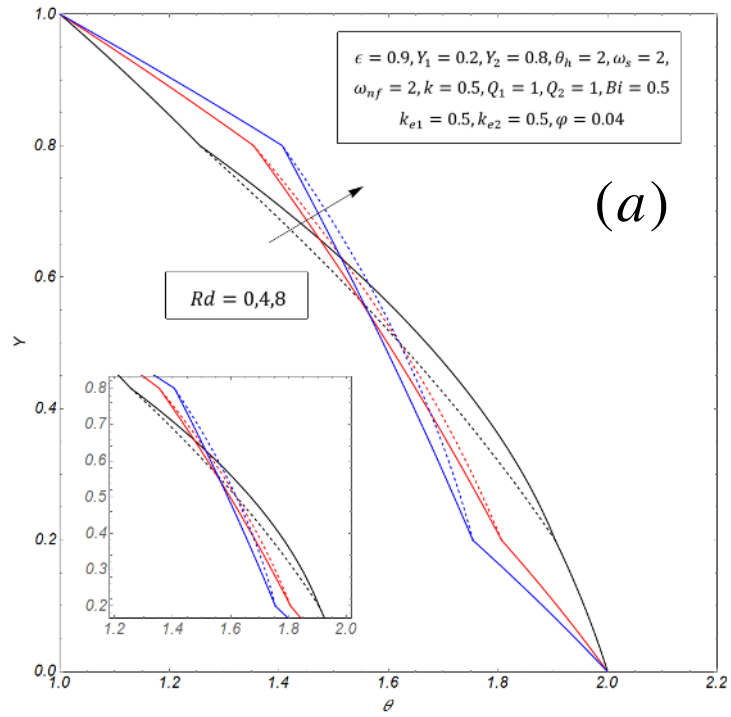**Fig. 1.** Schematic configurations of the model microreactors for (a) Case one and (b) Case two.
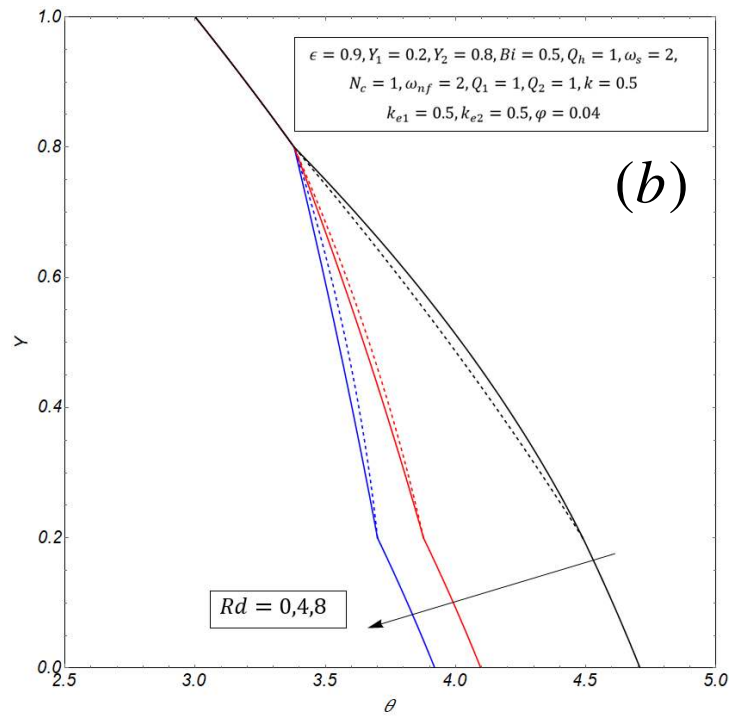
Fig. 2. Temperature distributions for different values for radiation parameter for (a) Case one and (b) Case two.
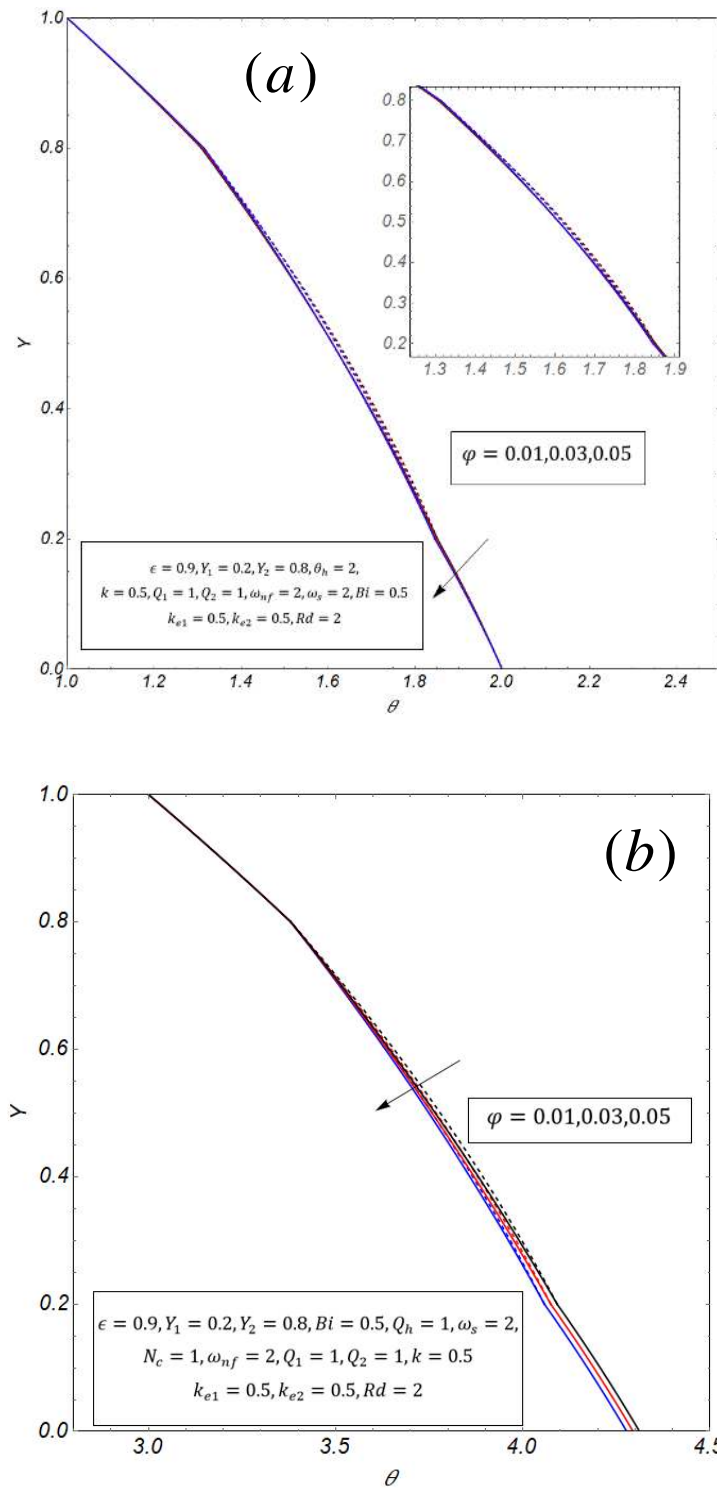
Fig. 3. Temperature distributions for different volumetric concentration of nanoparticles for (a) Case one and (b) Case two.
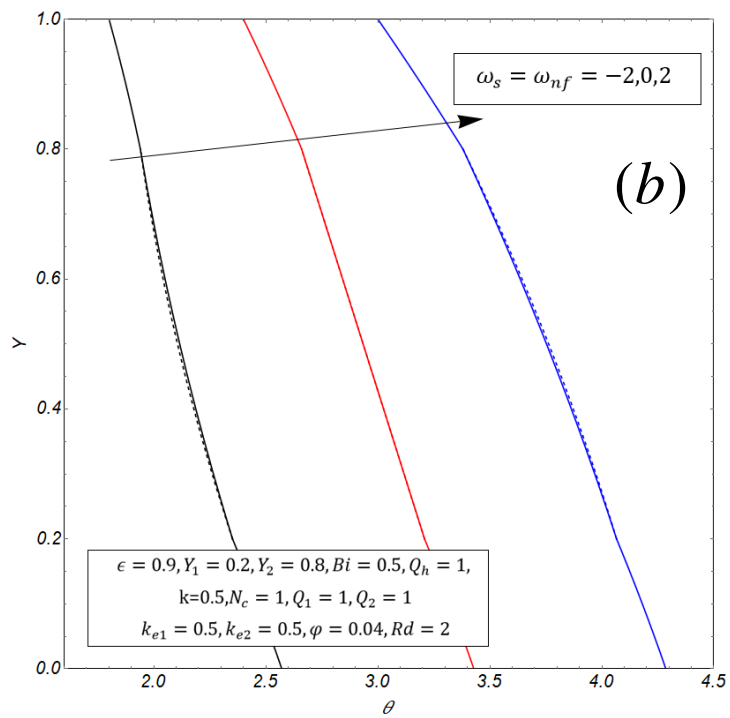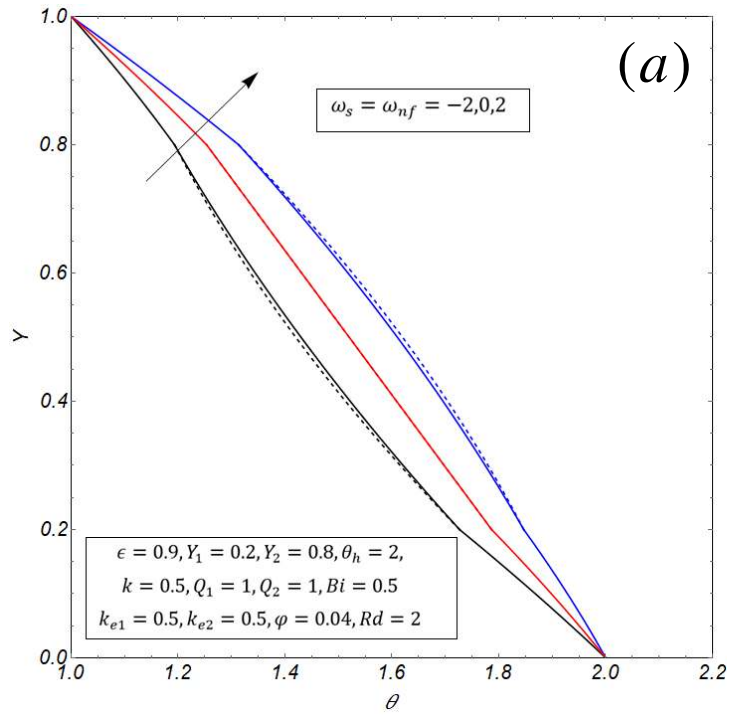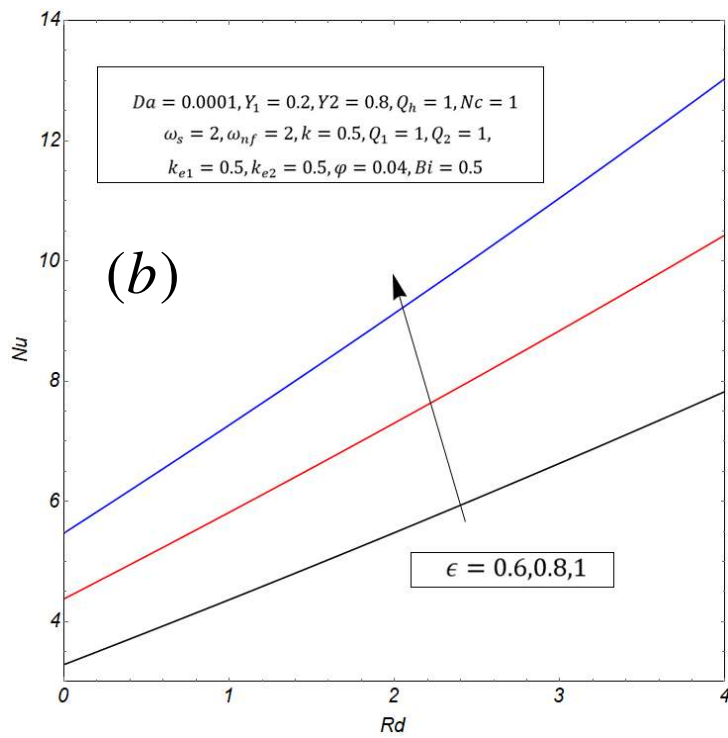
Fig. 4. Temperature distributions for different values of internal heat generation for (a) Case one and (b) Case two.
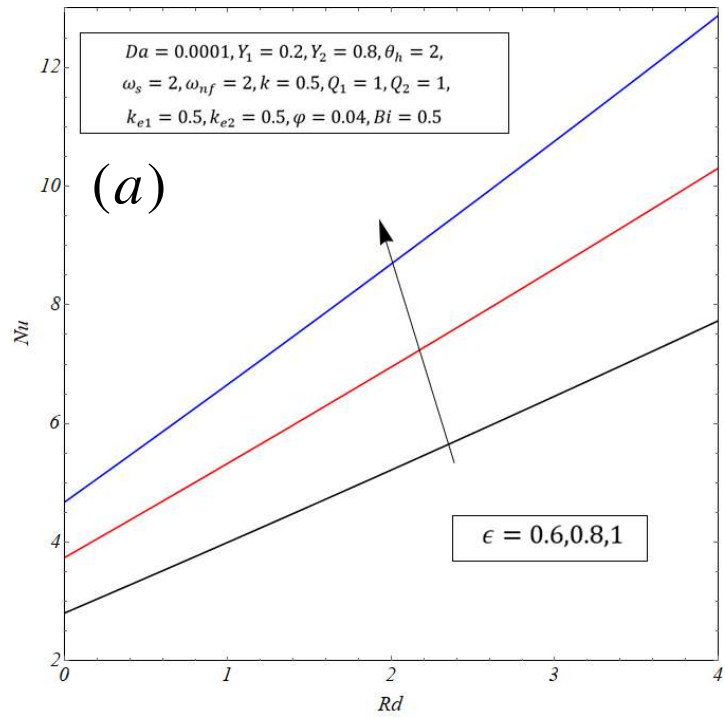
Fig. 5. Nusselt number versus radiation parameter for different values of porosity for (a) Case one and (b) Case two.
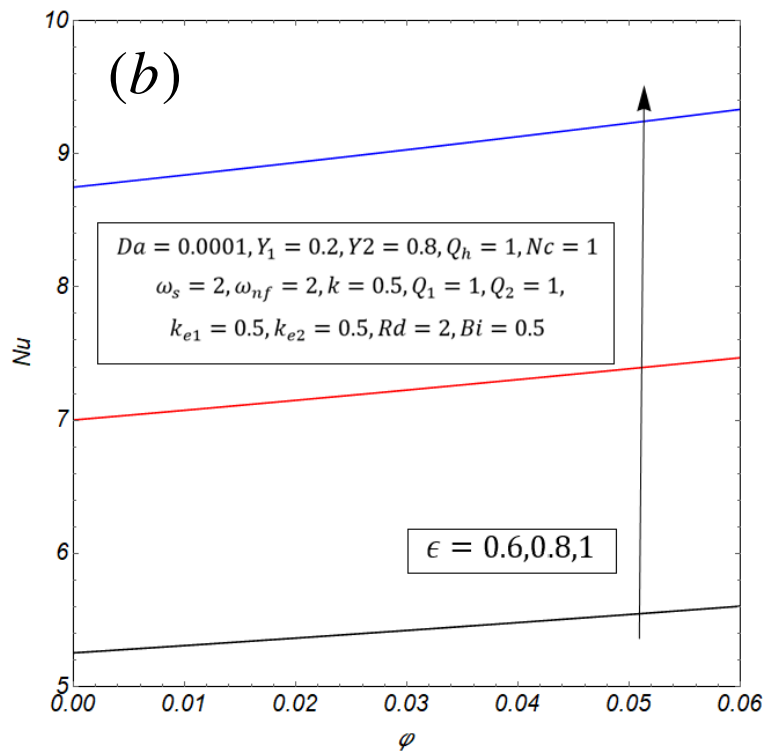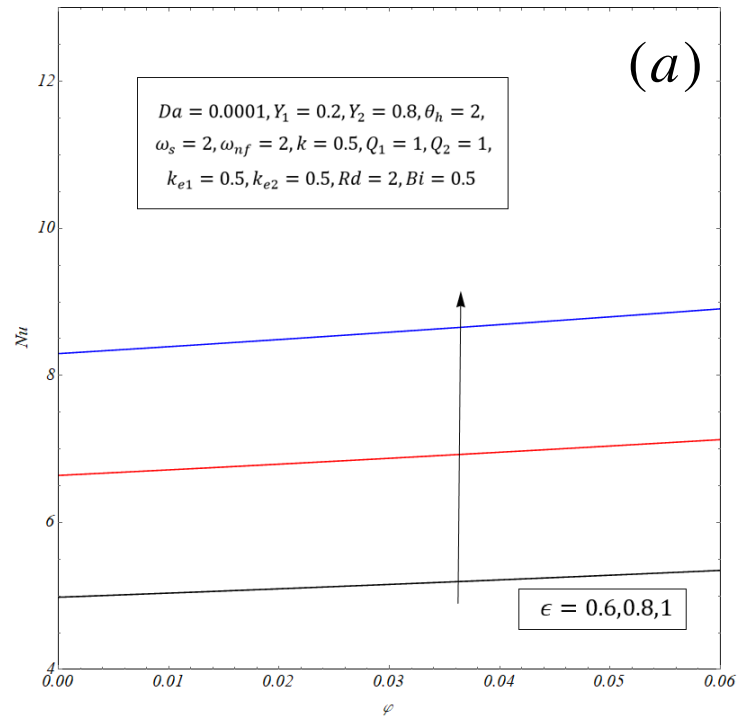
Fig. 6. Nusselt number versus volumetric concentration of nanoparticles and for different values of porosity for (a) Case one and (b) Case two.
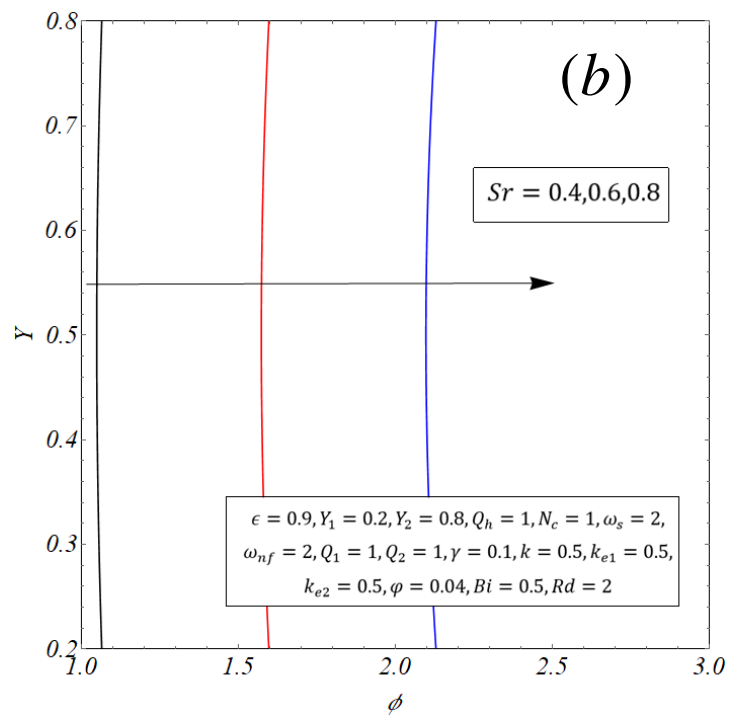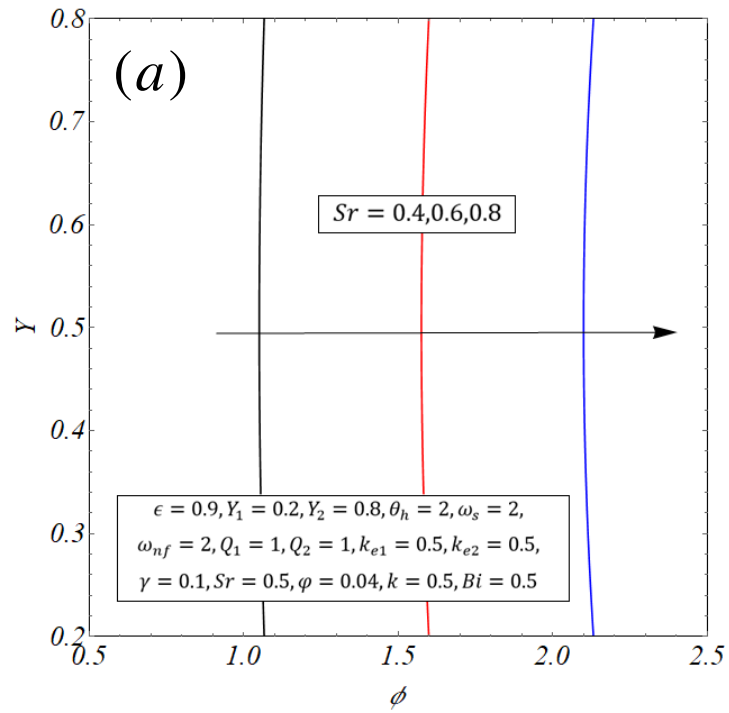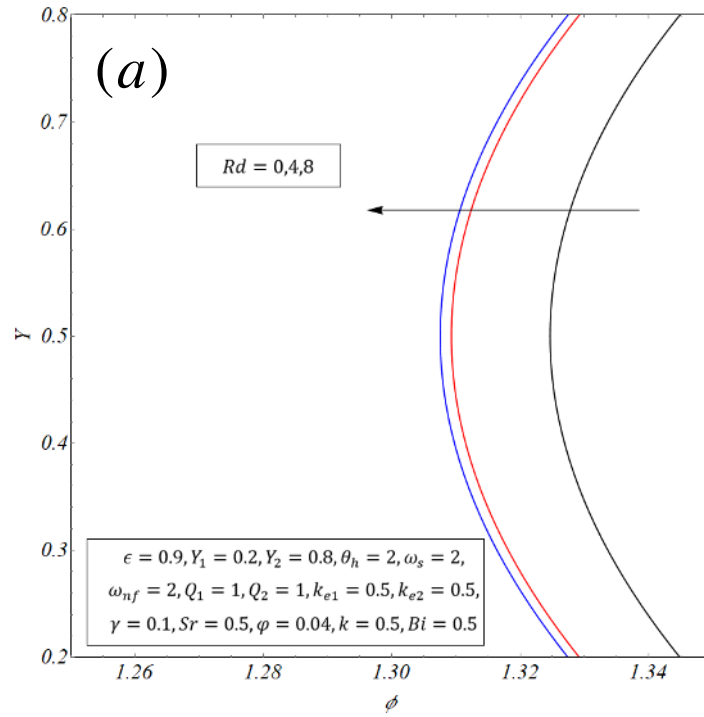
Fig. 7. Concentration distribution for different values of Soret number for (a) Case one and (b) Case two.
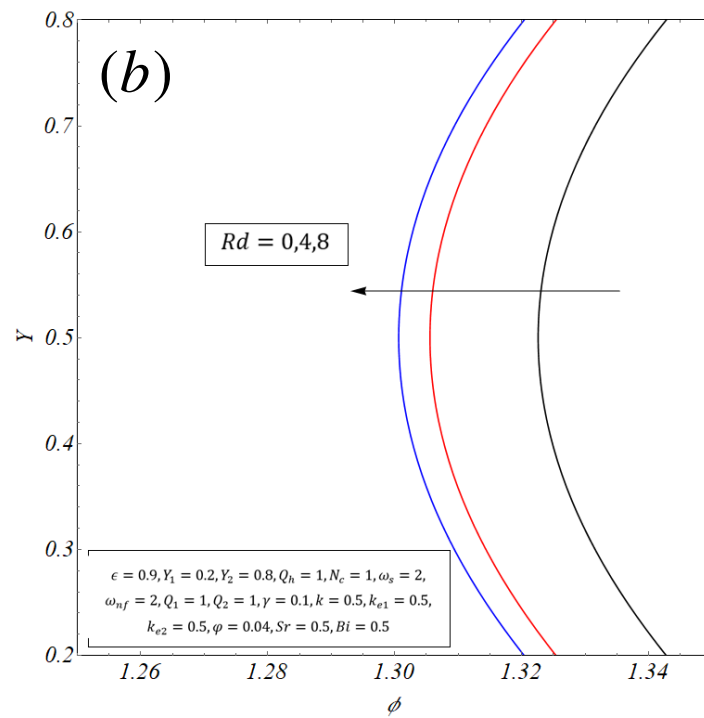
Fig. 8. Concentration distribution for different values of radiation parameter for (a) Case one and (b) Case two.
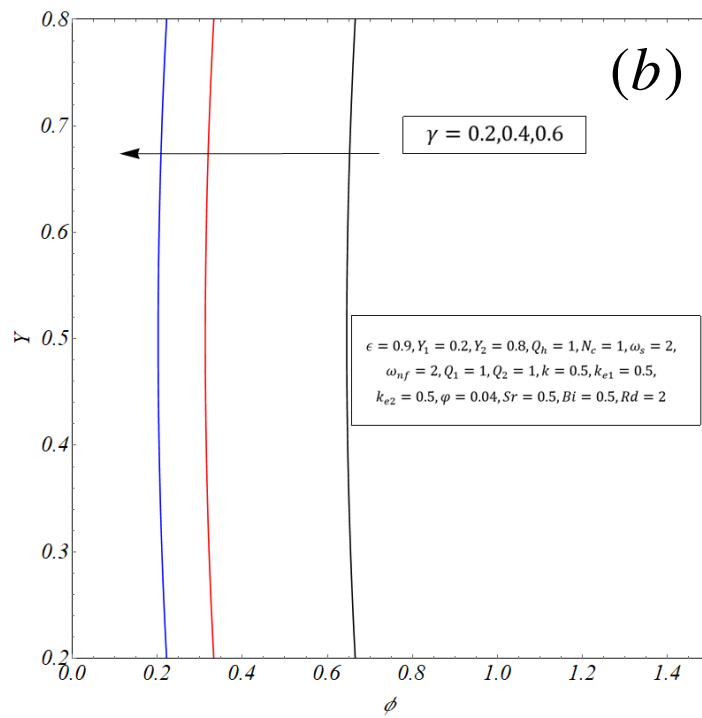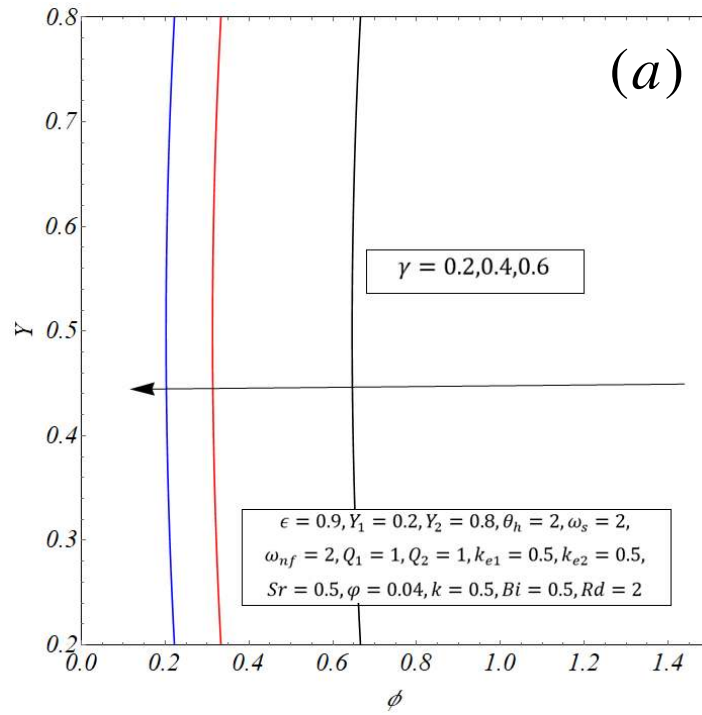
Fig. 9. Concentration distribution for different values of Damköhler parameter for (a) Case one and (b) Case two.